Longitude Structure of Wavenumber 4 of the Ionosphere after Midnight Based on the OI135.6 nm Night Airglow Using FY-3D Ionospheric Photometer

Bin Zhang[1,2,3,4], Liping Fu[1,3,4,*], Tian Mao[5,6,*], Xiuqing Hu[5,6], Yungang Wang[5,6], Fang Jiang[1,3,4], Nan Jia[1,2,3,4] , Tianfang Wang[1,2,3,4], Ruyi Peng[1,3,4] and Jinsong Wang[5,6]

[1]National Space Science Center, Chinese Academy of Sciences, Beijing 100190, China

[2]University of Chinese Academy of Sciences, Beijing 100190, China

[3]Beijing Key Laboratory of Space Environment Exploration, Beijing 100190, China

[4]Key Laboratory of Environmental Space Situation Awareness Technology, Beijing 100190, China

[5]Key Laboratory of Space Weather, National Satellite Meteorological Center (National Center for Space Weather), Beijing 100081, China

[6]Innovation Center for FengYun Meteorological Satellite (FYSIC), Beijing 100081, China

Corresponding author: Liping Fu;Tiao Mao (fuliping@nssc.ac.cn; maotian@cma.gov.cn)

Key Points:

- The wavenumber 4 longitudinal structures of EIA still exist after midnight and are more obvious at equinoxes
- The wavenumber 4 component of EIA after midnight is positively correlated with the solar activity level
- The origin of the wavenumber 4 longitudinal structures of EIA after midnight is the modulation of the transequatorial neutral wind

Abstract

In this study, based on the OI135.6 nm night airglow data of the FY-3D Ionospheric Photometer (IPM) during the 2018-2021 geomagnetically quiet period, the global wavenumber 4 longitudinal structure of the equatorial ionization anomaly (EIA) at 2:00 local time was discovered, and the component of the wavenumber 4 was extracted from these structures. Compared with the OI135.6 nm night airglow data of the Special Sensor Ultraviolet Spectrographic Imager (SSUSI) F18 during 2011-2014, there were significant differences in the variation pattern of the relative amplitude of the two versus solar activity and the seasonal variation in the proportion of the component of the wavenumber 4. Based on the neutral wind speed observation results of Global High-Resolution Thermospheric Imaging (MIGHTI) on board the Ionospheric Connection Explorer (ICON) from 2020-2021, the longitudinal structures of the 4 ionospheric waves after midnight are related to the cross-equatorial meridional wind. We believe that the wavenumber 4 longitudinal structures after midnight originate from the eastward nonmigrating tidal semidiurnal wave (SE2) with a wavenumber of 2 in the cross-equatorial neutral wind rather than the eastward nonmigrating tidal semidiurnal wave (DE3) with a wavenumber of 3 in from the zonal wind, which modulates the daytime wavenumber 4 longitudinal structures.

Plain Language Summary

The longitudinal structures of EIA has been extensively studied by using satellite data. However, there are few observations and studies, due to the weak ionosphere near midnight. In this paper, we studied the longitudinal structures of EIA at 02:00 local time during geomagnetically quiet period, benefitted from the satellite orbits and high sensitivity of FY-3D IPM. We found that the wavenumber 4 longitudinal structures of EIA still exist at 02:00 local time and are obvious at equinoxes. Compared with SSUSI F18 data, FY-3D IPM data showed different characteristics of wavenumber 4 component of EIA longitudinal structures.Since the different local time of data between SSUSI F18 and FY-3D IPM, we consider that the longitudinal wavenumber 4 structures of EIA after midnight originated from the cross-equatorial neutral wind rather than the electric field modulated by zonal neutral wind in daytime.

1.Introduction

EIA in the low-latitude F region ionosphere has been studied extensively. EIA is generally considered to be the result of the fountain effect, which is driven by the upward vertical E×B plasma drift caused by the eastward electric field E near the magnetic equator. As the plasma moves to a higher altitude, due to the pressure gradient force and gravity, it disperses along the geomagnetic field lines on both sides of the magnetic equator(Anderson, 1973; Duncan, 1960; Rishbeth, n.d.). Eventually, these processes generate a plasma density trough around the magnetic equator and two EIA peaks on both sides of the magnetic equator(Martyn, n.d.; Croom et al., 1959).

At night, the ionosphere O+ recombines with electrons or O- to generate excited-state atomic oxygen (O*); the 5S-3P transition of O* generates radiation at 135.6 nm, and the radiation intensity is proportional to the square of the oxygen ion O+ density(Meier, n.d.). Since the oxygen ion O+ is the most important component of the ionosphere, it can be approximated as $n_{o+} = n_{e-}$; thus, the radiation intensity of the 135.6 nm band is proportional to the square of the electron density. Therefore, 135.6 nm airglow detection in the nighttime ionosphere is an important means for studying the nighttime ionosphere.

$$I_{OI135.6}(z_0) \propto \int_0^{z0} n_{e-}^2 dz$$

Where z_0 is the altitude of the satellite, $I_{OI135.6}(z_0)$ is the radiation intensity of the OI 135.6 nm and n_{e-} is the electron density at altitude z.

Observations of the ionosphere by space-based optical remote sensing have good spatiotemporal continuity and can compensate for the shortcomings of the lack of ground-based stations for the ground surface and ocean. In the past few decades, the observation of OI 135.6 nm radiation intensity through remote sensing has become the main and most widely used optical means for the observation and quantification of ionospheric plasma parameters(Barth & Schaffner, 1970; Christensen, 2003; DeMajistre, 2004; Dymond et al., 1997; Jiang, Mao, Zhang, Wang, Hu, et al., 2020; Kamalabadi et al., 1999, 2002; Kil et al., 2004; Meier et al., 2015; Paxton et al., 1999).

For the first time, Sagawa used the FUV payload on IMAGE to detect OI 135.6 nm radiation intensity data and discovered the wavenumber 4 longitudinal structure of EIA at night(Sagawa et al., 2003). Several studies have summarized the pattern and explained the causes of the EIA wavenumber 4 longitudinal structure. Later, it was found that ionospheric parameters, including electron temperature, electron density, ion density, drift velocity, and F2-layer peak height, also have a wavenumber 4 longitudinal structure(Pacheco & Yizengaw, 2013; Pancheva & Mukhtarov, 2010; Ren et al., 2008, 2009; Scherliess et al., 2008b). Further study by Immel revealed that the EIA wavenumber 4 longitudinal structure can be explained by the interaction between daytime tidal waves and the E-layer dynamo; that is, the longitudinal variation in the EIA is caused by the tidal forcing of the lower atmosphere tides on the upper atmosphere(Immel et al., 2006). England used the IMAGE/FUV and TIMED/GUVI after-sunset EIA observation data for comparison with the noontime equatorial electrojet (EEJ) observations by CHAMP, Ørsted, and SAC-C and revealed that there was a geomagnetically quiet period around the vernal equinox. The EIA and EEJ showed very similar wavenumber 4 longitudinal structures, indicating strong vertical coupling between the ionosphere and troposphere because the longitudinal structure of the wavenumber 4 is driven by the troposphere(England et al., 2006). Lasker used the data of the GOLD satellite to study the early morning ionospheric EIA phenomenon in the Americas and combined with the simulation results of the WACCMX model, the results showed that the early morning EIA phenomenon had similar characteristics to the longitudinal structure of the wavenumber 4. They considered that the early morning EIA phenomenon was driven by low atmospheric waves(Laskar et al., 2020). Using SUSSI F18 data, Guo obtained the seasonal variation pattern of the amplitude and phase of the EIA wavenumber 1-4 components at 20:00 local time(Guo et al., 2020). Lin used the radio occultation observation data of FORMOSAT-3 to statistically study the local time pattern of the generation, continuation, and disappearance of the EIA longitudinal structure of the wavenumber 4 (Lin et al., 2007); however, an explanation of its origin is lacking. For the ionosphere between midnight and early morning, satellite observation data are lacking, and there are relatively few studies on the longitudinal structure and driving sources of EIAs. In this study, the longitudinal structure of the EIA after midnight was analyzed, and the fluctuation component was extracted. Then, the fluctuations in the current EIA in different areas were analyzed and explained based on the optical remote sensing data of the SSUSI F18 satellite and the neutral wind speed data of ICON.

2.Data Processing

The ionospheric photometer (IPM) onboard on the FY-3D meteorological satellite is an optical remote sensing payload that detects airglow radiation in the far-UV band of the thermosphere/ionosphere. By in-orbit monitoring of the OI135.6 nm and N2LBH (145.0-180.0 nm) radiation spectra, physical parameters, such as ionospheric total content (TEC), peak electron density (NmF2) and ionospheric O/N2, are retrieved at night(Jiang, Mao, Zhang, Wang, Fu, et al., 2020; Jiang, Mao, Zhang, Wang, Hu, et al., 2020; Wang D. et al., 2021; Y. Wang et al., 2021). On November 14, 2017, the FY-3D satellite was launched at an altitude of 830 km in a sun-synchronous orbit, and the ascending node local time of the satellite was 14:00. The load performance indicators of the ionospheric photometer are shown in Table 1[29]:

Table 1. The performance of FY-3D IPM.

Parameter	value
Wavelength	135.6 nm (night mode) 135.6 nm and 145–180 nm (day mode)
Field of view	$\sim 3.5°$ (along orbit) $\times$ $1.6°$ (cross orbit)
Sensitivity	day mode: $\geq$ 1 counts/s/Rayleigh at 135.6 nm night mode: $\geq$ 150 counts/s/Rayleigh at 135.6 nm
Spatial resolution	$\sim$ 30 km at ionosphere (300 km)
Time resolution	2 s (day mode) 10 s (night mode)

The Ionospheric Connection Explorer (ICON) was launched on October 10, 2019. The MIGHTI instrument was used on the satellite to measure the temperature and neutral wind of the upper atmosphere (Englert et al., 2023; Harlander et al., 2017). The MIGHTI wind speed observation is based on the Doppler frequency shift in the atomic oxygen red line at 630.0 nm (O(1D→3P) and the green line at 557.7 nm (O(1S→1D)). The height range of the red line is approximately 150-310 km. The height of the green line is in the range of 90 to 310 km, with a step size of 3 km. In this paper, the emission data of the Green Line with a larger height range and better vertical resolution, i.e., MIGHTI-green level 2.2 version 5, were used.

Special Sensor Ultraviolet Spectrographic Imager (SSUSI) is onboard the Defense Meteorological Satellite Program (DMSP) F18 satellite and was launched on October 18, 2009. The satellite has a sun-synchronous orbit with an altitude of nearly 840 km, an inclination of 98.7°, and a period of approximately 104 minutes (with an average of 14 revolutions/day). The time required to reach the equator is basically fixed at 08:00/20:00. SSUSI is an optical remote sensing instrument that measures UV radiation and visible light (airglow and surface albedo) from the atmosphere and ionosphere. The instrument regularly provides maps of the composition of the ionosphere and upper atmosphere, as well as images of the aurora borealis(Paxton et al., 1992, 2002). The local time difference between the SSUSI F18 and FY-3D IPM can be used to compare the characteristics of the ionospheric wavenumber 4 longitudinal structure at different local times.

For the FY-3D IPM and SSUSI F18 data, the nighttime data collected during the geomagnetically quiet period were chosen in this study. Summing the 8 K_p values for each day yields $\sum K_p$, $\sum K_p$ <20 and each K_p of the remaining days (<5) were considered as geomagnetically quiet days. The OI135.6 nm radiation intensity distribution at 2 a.m. during the quite period was obtained by plotting the data for one month.

The areas covering -180°~180° longitudes and -40°~40° latitudes were divided into a 4°×4° grid, and then, the IPM data of each monthly geomagnetic quiet period FY-3D were averaged in the grid. The mesh distribution diagram of the OI135.6 nm radiation intensity for the corresponding month was obtained(Zhang et al., 2022).

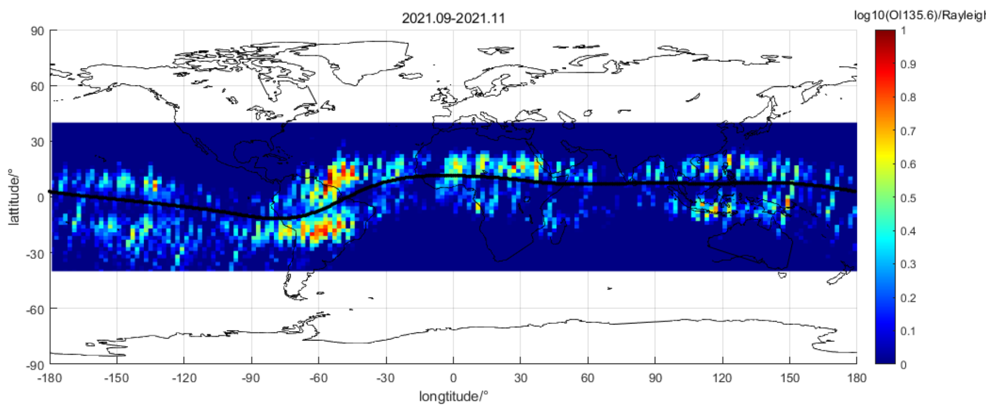

Figure 1. Schematic diagram of the OI 135.6 nm radiation intensity near 2:00 local time from September to November 2021

In Fig. 1, the abscissa represents the longitude, the vertical axis represents the latitude, the color represents the OI 135.6 nm radiation intensity, and the unit is Rayleigh. The black line is the geomagnetic equator. Figure 1 shows the gridded OI135.6 nm radiation intensity distribution during the geomagnetic quiet period from September to November 2021. The figure shows that the EIA is symmetric on both sides of the geomagnetic equator, and there is a significant variation in the EIA intensity versus the wavenumber 4 longitudinal structure. The position of the EIA peak is usually limited to within ±(10°-20°) geomagnetic latitudes, and most are at approximately ±15° geomagnetic latitude (Lühr et al., 2007; Scherliess et al., 2008a; Sunda & Vyas, 2013). Fig. 1 shows that the magnetic latitude of the EIA is lower after midnight. Therefore, in the present study, the ±10° magnetic latitude was taken as the latitudinal area of the EIA peak to obtain the distribution of the strength versus longitude of the EIA peak and perform the smoothing processing. The EIA peak intensity was fitted by the sum of triangular functions, and the fitting function is shown as follows:

$$I_{oi135.6} = \sum_{i=1}^{4} A_i \cos\left(\frac{2\pi}{360} * i * (x - f_i)\right) + k$$

$I_{oi135.6}$ is the OI135.6 nm radiation intensity, and k is the residual term. A_i and f_i are the amplitude and initial phase of the fluctuation component i (Guo et al., 2020), respectively. The data used in this paper included four years of data from January 2018 to December 2021. EIA-N is the northern EIA crest, and EIA-S is the southern EIA crest.

3.Results and Discussion

The FY-3D IPM nighttime airglow data on geomagnetically quiet days were selected and gridded to obtain the global monthly variation map of the airglow intensity at mid-to-low-latitudes. Wavenumber 1-4 components were extracted from the EIA area, and the amplitudes of wavenumber 1-4 components and the F10.7 index were plotted monthly. The results are shown in Figure 2.

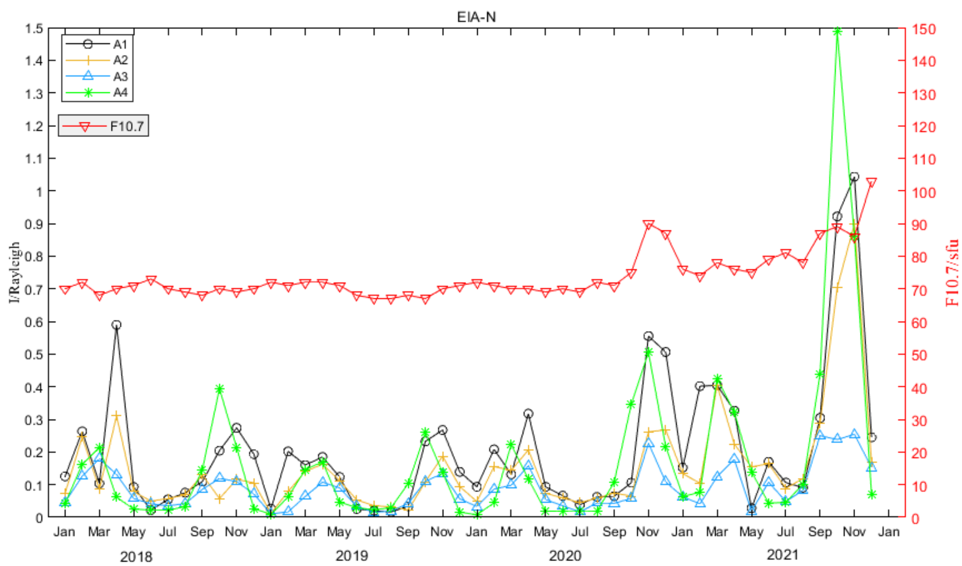

(a)

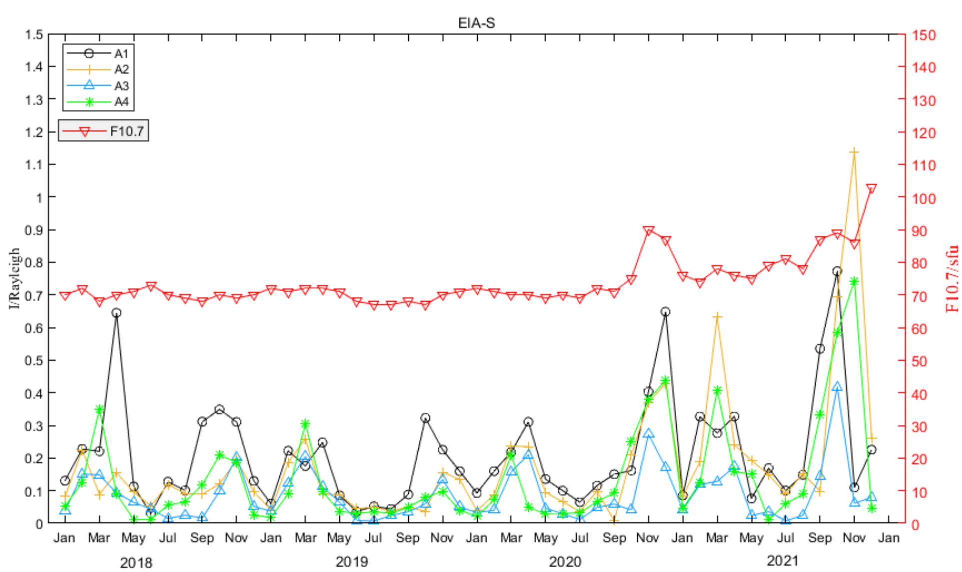

(b)

Figure 2a, b Schematic diagrams of the seasonal variations in the amplitude of wavenumber 1-4 versus the F10.7 index in the Northern Hemisphere (a) and Southern Hemisphere (b) during 2018-2021.

In Fig. 2, the black line, yellow line, blue line, and green line are the seasonal variation curves of the amplitudes of wavenumber 1-4; the red line is the seasonal variation curve of the F10.7 index. Figure 2a shows the Northern Hemisphere, and Figure 2b shows the Southern Hemisphere. The figure shows that the amplitudes of wavenumber 1-4 in the Northern and Southern Hemispheres all have a period of approximately 6 months, the peak values are located near the equinoxes (April and October), and the amplitudes increase with increasing F10.7 (solar activity). Especially from November to December 2020, the F10.7 index temporarily increased, and the amplitudes of wavenumber 1-4 during this period were also stronger than those during the same period in previous years. Moreover, the amplitude in November was greater than that in October.

The ionosphere level is strongly modulated by solar activity. Higher solar activity will cause a stronger ionospheric level, which in turn will affect the amplitude of fluctuations in the EIA. Therefore, we use the relative amplitude to remove the effect of the ionospheric background strength, which is defined as the ratio of the amplitude to the background strength, that is, A_i/k. Consider the seasonal variation in the relative amplitude A_4/k of the wavenumber 4, as shown in Figure 3 below:

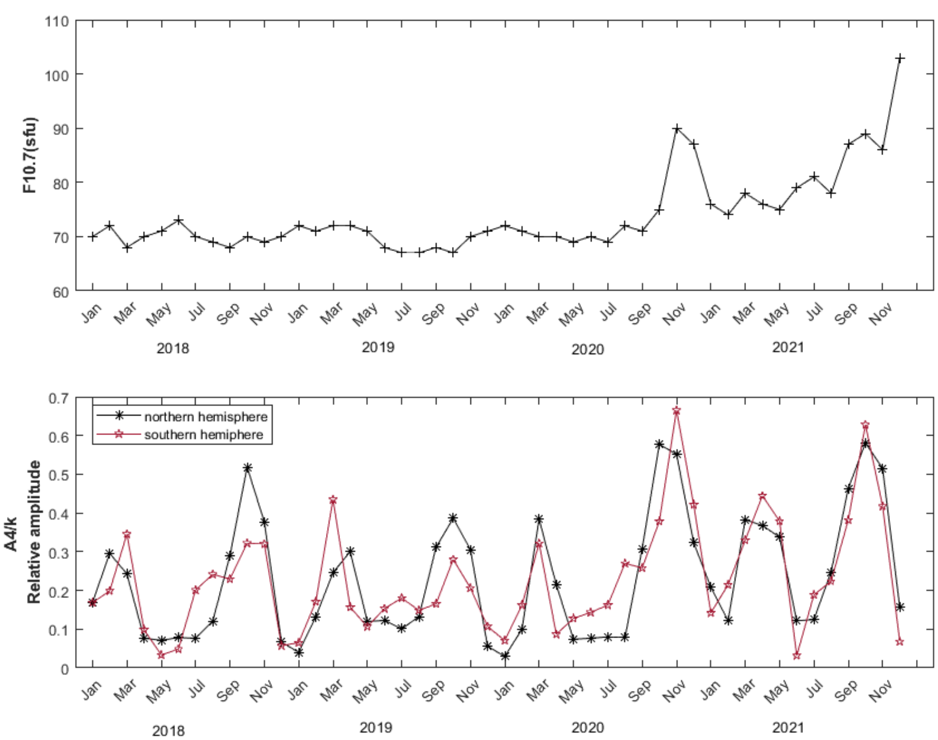

Figure 3. Variation of the F10.7 index (the upper) and relative amplitude of the EIA wavenumber 4 component (the bottom) during 2018 to 2021.

Figure 3 shows the variation diagram of the F10.7 exponential intensity. The horizontal axis represents the time in months, and the vertical axis represents the F10.7 radiation intensity. Figure 3b is the seasonal variation diagram of the relative amplitude of the EIA wavenumber 4 component, with the horizontal axis showing the unit of month. The vertical axis is the relative amplitude of the EIA wavenumber 4 component.

Figure 3 shows that after conversion to relative amplitude, the EIA wavenumber 4 component still has a period of approximately half a year, with peak values occurring near the equinoxes (April and October), and the relative amplitude of the peak near October is greater than that around April. The F10.7 index in November 2020 and October 2021 was greater than that in the same period in previous years. During these two-month periods, the relative amplitude of the EIA wavenumber 4 component was also the highest in the same period in previous years.

In the following section, we include a paragraph about the relationship with longitude.

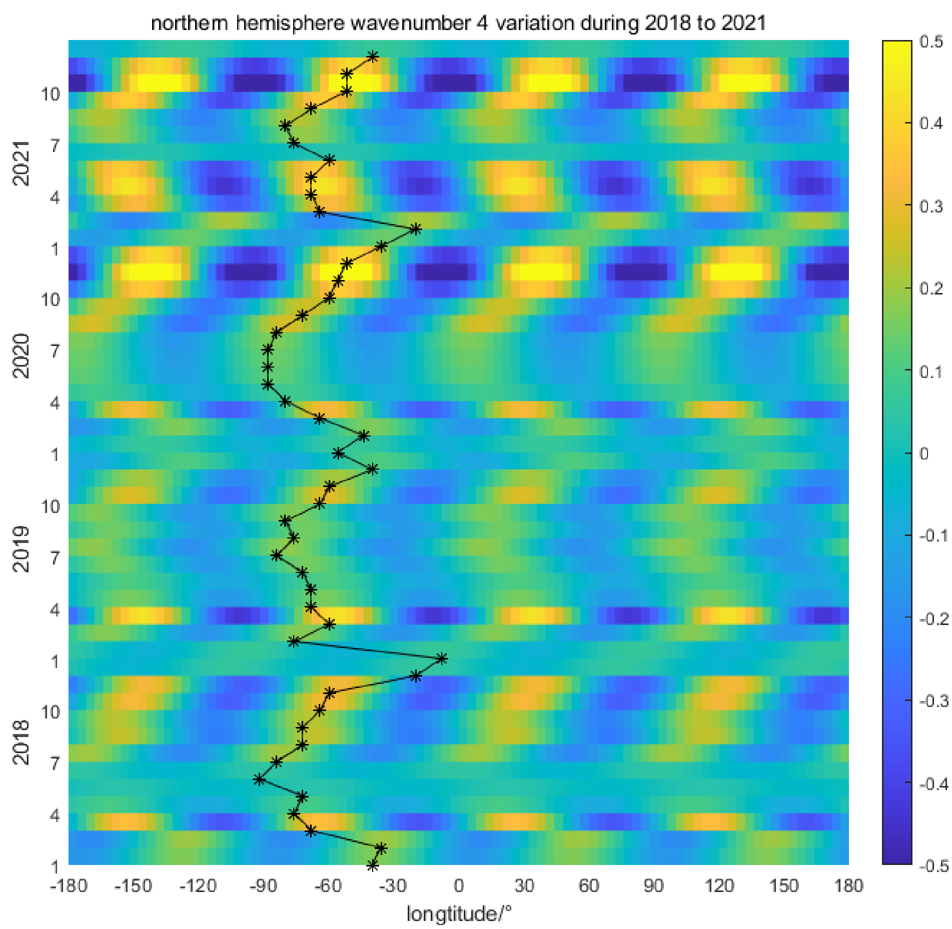

(a)

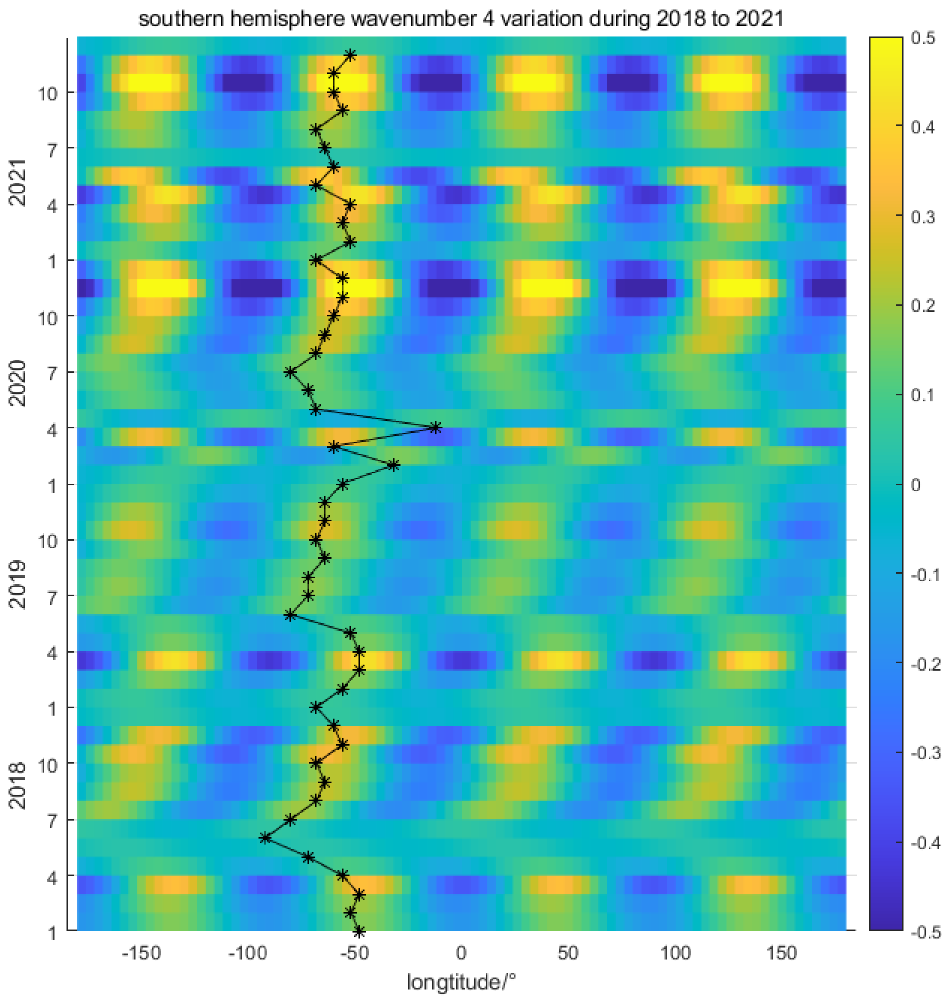

(b)

Figure 4. Seasonal-longitude variation diagram of the relative amplitude of the EIA wavenumber 4 component in the Northern Hemisphere (a) and Southern Hemisphere (b).

Figure 4 shows the season-longitude distribution diagram of the relative amplitude of the EIA wavenumber 4 component. The horizontal axis is the geographic longitude, and the vertical axis is the time in months. The color represents the relative amplitude of the EIA wavenumber 4 component. The black line indicates the seasonal variation curve of the peak position of the EIA wavenumber 4 component. Fig. 4a shows the results for the Northern Hemisphere, and Fig. 4b shows the results for the Southern Hemisphere.

Fig. 4 shows that since October 2020, the relative amplitude of the EIA wavenumber 4 component has significantly increased compared to that of the previous component, and the solar activity level modulates the intensity of the wavenumber 4 component in the EIA. The above characteristics were consistent in the Northern and Southern Hemispheres. The difference is that in the Northern Hemisphere, the position of the wave crest varies seasonally: from January to July, the wave crest moves westward and then moves eastward from July to December. In the Southern Hemisphere, in most months, the position of the wave crest remains relatively stable.

To study the temporal wavenumber 4 longitudinal distribution at different locations, we analyzed the nighttime 135.6 nm airglow data from the SSUSI F18 in the same way, in addition to data was divided into 1°×1° grid. We chose the night data from 2011 to 2014 for this payload rather than the data of the same year as FY-3D because between 2018 and 2021, the local time of the equator of the DMSP F18 drifts every year. At different local times, the fluctuation structure in the EIA varies (Pacheco & Yizengaw, 2013). Therefore, we chose the data from 2011 to 2014, when the solar activity level was also in the rising stage and local time drift did not occur.

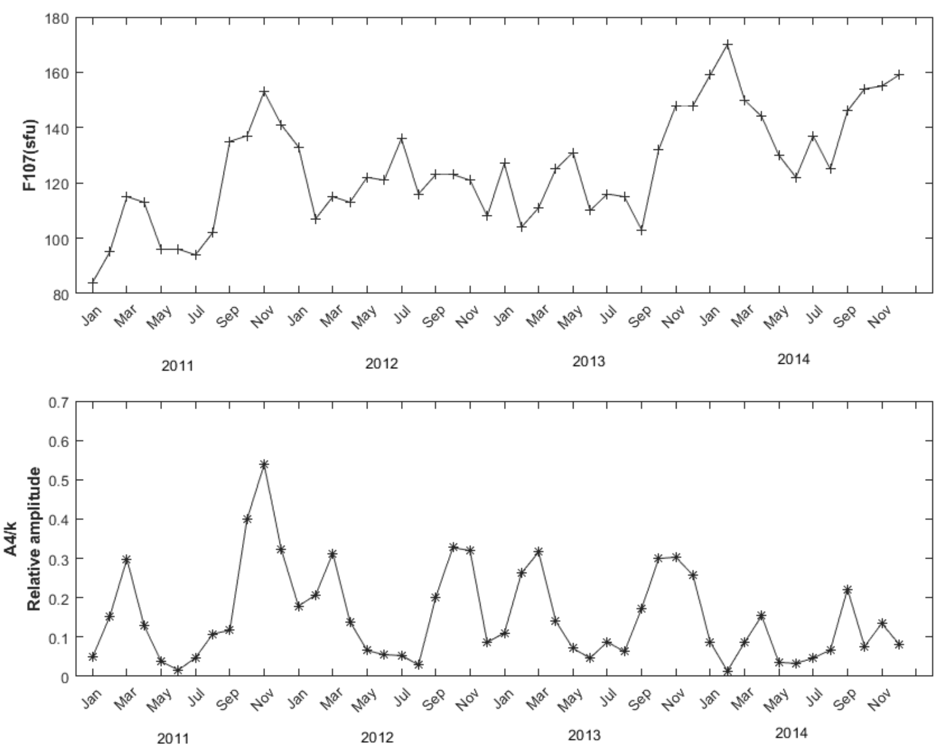

(a)

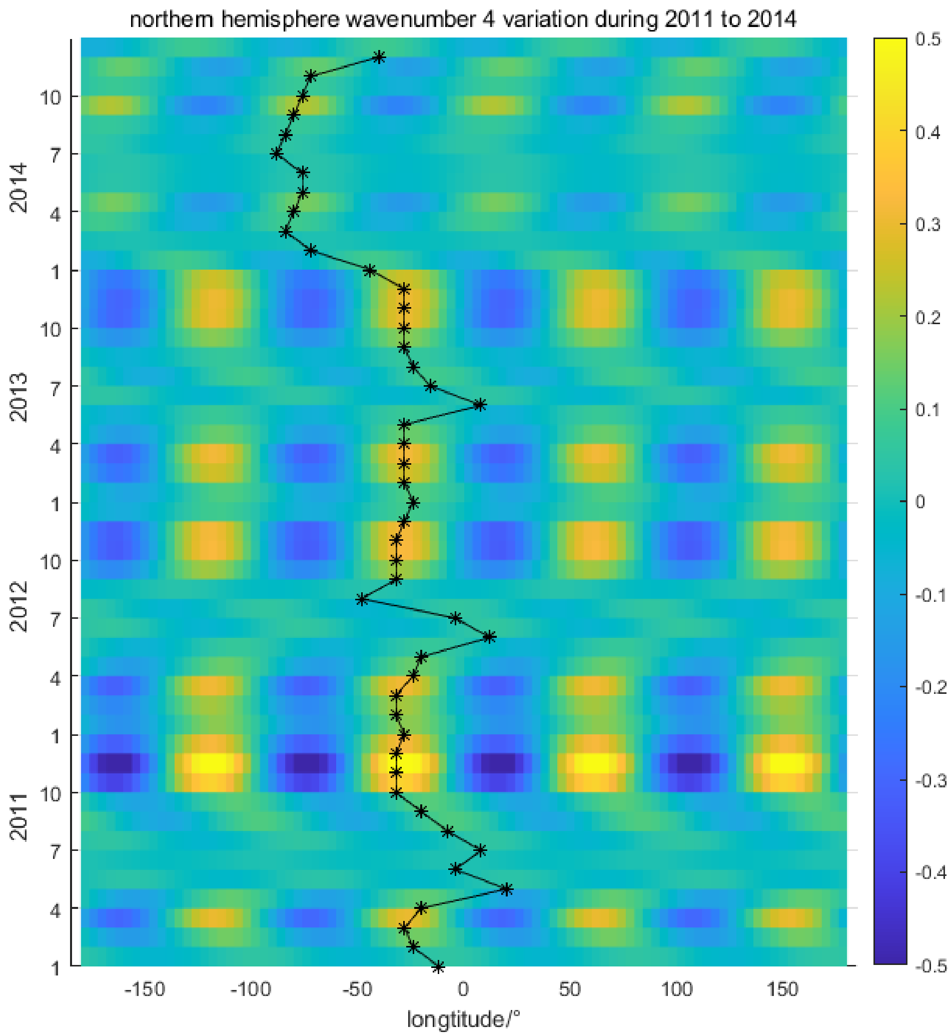

(b)

Figure 4a. Variation of the F10.7 index (the upper) and relative amplitude of the EIA wavenumber 4 component (the bottom) during 2011 to 2014. **Figure 4b.** Seasonal-longitude variation in the relative amplitude of the EIA wavenumber 4 component for the Northern Hemisphere during 2011-2014

In Fig. 4, based on the OI135.6 nm airglow data of the SSUSI F18 from 2011 to 2014, the relative amplitude of the EIA wavenumber 4 component was extracted using the same processing method as that used with the FY-3D IPM data described above.

Figure 4a shows that the F10.7 indices of November 2011 and November 2014 were similar. However, the relative amplitudes of the EIA wavenumber 4 component extracted from the

SSUSI data differ significantly. In 2014, the F10.7 index increased significantly, reaching the highest level in all four years. However, the relative amplitude of the EIA wavenumber 4 component at the equinox was the lowest over the 4 years. Due to the presence of the South Atlantic anomalous area in the Southern Hemisphere, the data quality of the SSUSI F18 is severely affected, so only the results for the Northern Hemisphere are shown in Fig. 4b. As shown in Fig. 4b, for the position of the peak in the wavenumber 4 component, during the period from 2011 to 2013, the peak moved eastward from April to July and westward from July to October, and the peak position in other months basically remained unchanged.

There were consistencies and differences between the FY-3D IPM and SSUSI F18 results. The consistencies are reflected in the fact that the relative amplitudes of the wavenumber 4 component all have a semiannual period, and they all reach their peaks at approximately 2 minutes. The differences are reflected in the relationship between the relative amplitude of the EIA wavenumber 4 component and solar activity and the seasonal variations in the wave crest positions in the Northern Hemisphere.

As shown in Fig. 1, after the FY-3D OI135.6 nm airglow data from September to November 2021 were gridded, the wavenumber 4 longitudinal structure of the EIA was very obvious. The four peaks were located in the Pacific Ocean region, the Americas region, the African region, and the Southeast Asian region. It is rare to obtain such a clear observation of the wavenumber 4 longitudinal structure of EIA around the world. For example, the significant EIA wavenumber 4 longitudinal structure cannot be directly observed in the gridded SSUSI F18 data. The main reason is that for the FY-3D IPM nighttime, the sensitivity is high, reaching 260 counts/s/R in the 135.6 nm band, and the local time is fixed; therefore, the distribution characteristics of weak airglow around midnight can be clearly displayed. Based on the 135.6 nm airglow data from the FY-3D IPM and the 135.6 nm night airglow data from the DMSP F18 SSUSI, we investigated the proportion of each EIA component and thus determined the reason why the EIA near October 2021 exhibited a clear wavenumber 4 longitudinal structure. The calculation formula is $w_i = \frac{A_i^2}{A_1^2+A_2^2+A_3^2+A_4^2}$, where i=1, 2, 3, 4. w_i is the proportion of the i-th component, and A_i is the amplitude of the i-th component.

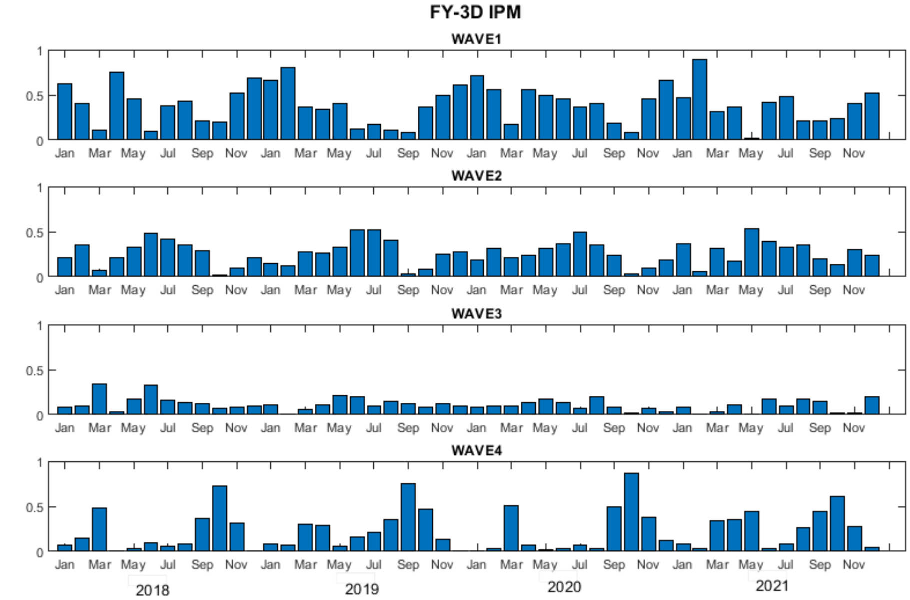

(a)

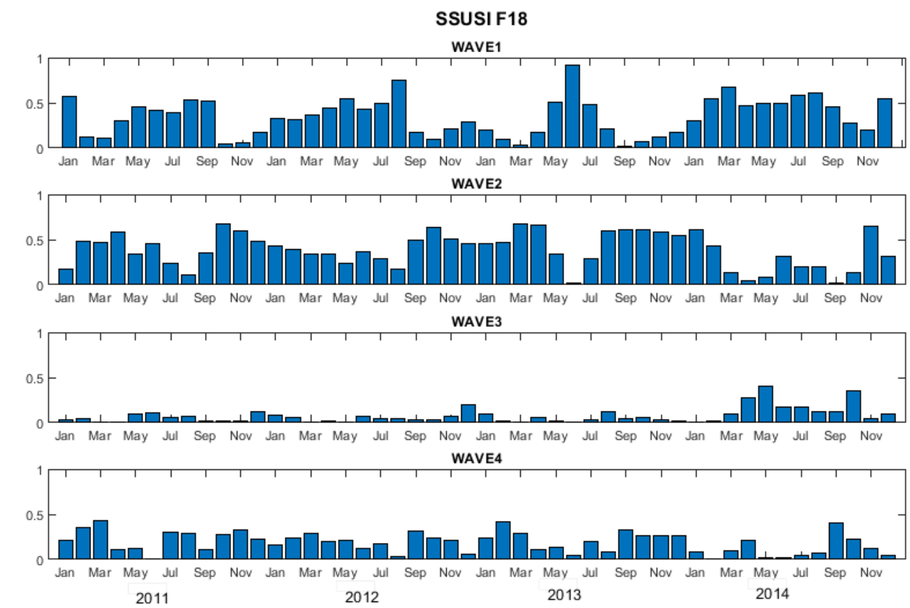

(b)

Figure 5a. Seasonal variations in the proportion of the EIA wavenumber 1-4 component based on FY-3D IPM data extraction. **Figure 5b.** Seasonal variation diagram of the proportion of the EIA wavenumber 1-4 components based on SSUSI F18 data extraction.

In Figures 5a and 5b, the horizontal axis represents the time in months, and the vertical axis represents the proportion. From top to bottom, they are wavenumber 1, wavenumber 2, wavenumber 3, and wavenumber 4. The FY-3D IPM and SSUSI F18 results showed both consistencies and differences. The consistencies were reflected in that in most months, wavenumber 1 and wavenumber 2 were the largest components, and wavenumber 3 was the smallest component. The differences are reflected in the fact that the proportion of wavenumber 4 in the FY-3D IPM results increases significantly, reaching approximately 50% near the vernal equinox and more than 70% near the autumnal equinox, becoming the largest proportion among the four components. At this time, the longitudinal structure of wavenumber 4 of the EIA was the most obvious, and the seasonal variation in the wavenumber 4 proportion showed a semiannual cycle. On the other hand, in the SSUSI F18 results, the seasonal variation in the wavenumber 4 proportion was irregular and always less than 50%.

The longitudinal structure of the wavenumber 4 of the ionosphere has been extensively studied. Eastward nonmigrating tidal waves with a wavenumber of 3 (DE3) from the thermospheric atmosphere are considered as the cause of the longitudinal structure of the wavenumber 4. In addition, for east nonmigrating tidal semicircular waves (SE2) with a wavenumber of 2, the stationary planetary wavenumber 4 SPW4 may also generate a longitudinal structure of wavenumber 4 in the ionosphere(He et al., 2011; Li et al., 2019, 2020; Lühr et al., 2007; Pancheva & Mukhtarov, 2010; Pedatella et al., 2008; Wan et al., 2010). In response to the difference between the FY-3D IPM and SSUSI F18 results, we studied the neutral wind conditions after midnight local time.

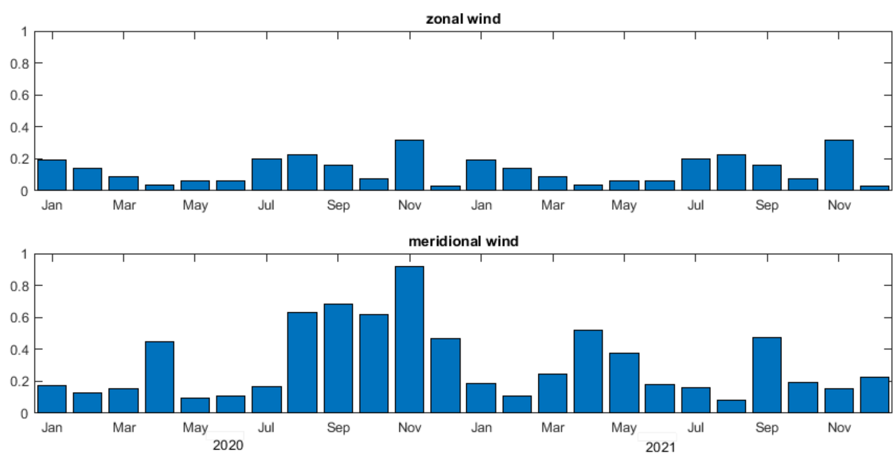

Figure 6. Seasonal variation diagram of the proportion of the wavenumber 4 component of the neutral wind at the geographic equator at 0-2:00 local time at an altitude of 300 km based on the ICON MIGHTI data.

Figure 6 is based on the ICON MIGHTI seasonal variation map of the wavenumber 4 component proportions extracted from the geographic equatorial neutral wind for the data from 0-2:00 during the 2020-2021 period. The first row is the seasonal variation map of the wavenumber 4 component proportion of the zonal component of the neutral wind, and the second row is the seasonal variation map of the wavenumber 4 component proportion of the neutral wind.

Fig. 6 shows that the proportion of the wavenumber 4 component in the zonal wind after midnight is very low, approximately 20%, and the maximum is less than 40%, while the wavenumber 4 component in the meridional wind account for a very high proportion. During the two-point period, it could reach more than 50%. The peak proportion in November 2020 was due to the sudden increase in solar activity that month. These results are close to the results of the wavenumber 4 component of the 5.6 nm airglow radiation of the OI observed with the FY-3D IPM.

Since Sagawa discovered the longitudinal structure of the wavenumber 4 of the ionosphere, many studies have attempted to explain its origin. The most common explanation is that the eastward nonmigrating tidal wave DE3 with wavenumber of 3 from the lower atmosphere propagates upward and modulates the E-region dynamo through the zonal wind, thereby affecting the fountain effect to form the longitudinal structure of the wavenumber 4 in the ionosphere. The electric field in Area E turns westward at night. Even if sunset inversion enhancement (PRE) at approximately 19 local times is considered, the eastward electric field in Area E after midnight inevitably disappears, and the fountain effect cannot be maintained. Therefore, the fluctuation structure in the zonal wind will not be transferred to the ionosphere. However, based on the FY-3D IPM observations, a clear longitudinal structure of the wavenumber 4 is found in the EIA after midnight. In addition, the relationships between the relative amplitude and solar activity, as well as the seasonal variations in the proportions of the wavenumber 4, are different from the results observed at SSUSI F18. The local time of the SSUSI F18 data is approximately 20:00, and its fluctuation structure is considered as the residual of the modulation of the generator in Area E by the zonal wind during the daytime after sunset. Therefore, we suspect that there are differences in the origin of the ionospheric longitudinal structure of the wavenumber 4 at 2:00 local time and the longitudinal structure of the wavenumber 4 of the ionosphere during the day. Based on the GOLD observations, the early morning ionospheric equatorial anomaly (EM-EIA) phenomenon was discovered in the early morning, and their simulations showed that under the conditions of a low solar year and geomagnetic quiet period, EM-EIA can occur worldwide, and its expression exhibits characteristics similar with those of the longitudinal structure of the wavenumber 4. These researchers believe that the EM-EIA is driven by dynamic changes related to lower atmospheric waves (Laskar et al., 2020b). He et al. (2011) studied the symmetry and anti-symmetry of the wavenumber 4 component of the peak electron concentration (Nmax) and peak electron height (HmF2) at different times based on the COSMIC dataset and reported that the wavenumber 4 component of the ionosphere near midnight can be explained by easterly nonmigrating tidal semicircular waves (SE2) with a wavenumber of 2 in cross-equatorial neutral winds (Ren et al., 2009). Based on the results shown in Figs. 3, 4, 5, and 6, the longitudinal structure of the wavenumber 4 of the ionosphere after midnight is significantly different from that during the day. The seasonal variation in the proportion of the wavenumber 4 component in the equatorial wind observed by ICON MIGHTI and the FY-3D IPM OI135.6 nm airglow observations are similar with each other, which supports the fact that the longitudinal structure of the wavenumber 4 of the ionosphere after midnight is modulated by the trans-equatorial neutral wind.

4. Conclusions

This paper used OI135.6 nm night airglow observation data collected during the 2018-2021 geomagnetically quiet period using the FY-3D IPM. We found that there was a clear longitudinal structure of wavenumber 4 in the EIA after midnight (2:00 local time), and we compared this finding with the observational results of the OI135.6 nm night airglow of the SSUSI F18. Based on the 2020-2021 neutral wind speed data of ICON MIGHTI, we made the following conclusions:

1. The longitudinal structures of the wavenumber 4 of the ionosphere may still exist after midnight and are more obvious at equinoxes.
2. After midnight, the wavenumber 4 component of the ionosphere are affected by solar activity, and the relative amplitude is positively correlated with the solar activity level.
3. The longitudinal structure of the wavenumber 4 of the ionosphere after midnight is caused by the modulation of the neutral wind across the equator rather than the modulation of the zonal wind during the day.

Since FY-3D satellite IPM data were released to the public in 2018, the data have not yet covered the entire solar activity cycle, and the statistical period between the ionospheric wavenumber 4 components and the solar activity level is relatively short. Currently, the IPM load is still operating normally, and the data will be further developed in the future. Relevant data should be analyzed to improve follow-up studies.

Acknowledgments

This study was supported by the National Key R & D Program of China (Grant No. 2022YFF0503901), and National Natural Science Foundation of China (NO. 42174226, 41874187). We gratefully acknowledge the Air Force Weather Agency and Ionospheric Connection Explorer and the Ionospheric Connection Explorer mission for providing SSUSI Level 1B data (https://ssusi.jhuapl.edu/data_availability) and ICON Level 2 MIGHTI data (ftp://icon-science.ssl.berkeley.edu/pub/LEVEL.2/MIGHTI/). We also thank the Space Weather Prediction Center (SWPC) at National Oceanic and Atmospheric Administration (NOAA) and World Data Center for Geomagnetism, Kyoto for providing F10.7 data (ftp://ftp.swpc.noaa.gov/pub/indices/old_indices/) and Kp data (https://wdc.kugi.kyoto-u.ac.jp/kp/index.html#LIST).

Data Availability Statement

The FY-3D data is provided from https://satellite.nsmc.org.cn/portalsite/default.aspx/ (accessed on 11 March 2024).

References

Anderson, D. N. (1973). A THEORETICAL STUDY OF THE IONOSPHERIC F REGION EQUATORIAL ANOMALY-I. THEORY. *Planetary and Space Science, 21(3)*, 409–419. https://doi.org/doi.org/10.1016/0032-0633(73)90040-8

Barth, C. A., & Schaffner, S. (1970). OGO 4 spectrometer measurements of the tropical ultraviolet airglow. *Journal of Geophysical Research, 75(22)*, 4299–4306. https://doi.org/10.1029/JA075i022p04299

Christensen, A. B. (2003). Initial observations with the Global Ultraviolet Imager (GUVI) in the NASA TIMED satellite mission. *Journal of Geophysical Research*, *108*(A12), 1451. https://doi.org/10.1029/2003JA009918

Croom, S., Robbins, A., & Thoma, J. O. (1959). Two anomalies in the behavior of the F2 layer of the ionosphere. *Nature*, *184(4704)*, 2003–2004. https://doi.org/10.1038/1842003a0

DeMajistre, R. (2004). Retrievals of nighttime electron density from Thermosphere Ionosphere Mesosphere Energetics and Dynamics (TIMED) mission Global Ultraviolet Imager (GUVI) measurements. *Journal of Geophysical Research*, *109*(A5), A05305. https://doi.org/10.1029/2003JA010296

Duncan, R. A. (1960). The equatorial F-region of the ionosphere. *Journal of Atmospheric and Solar-Terrestrial Physics*, (18(2–3)), 89–100. https://doi.org/10.1016/0021-9169(60)90081-7

Dymond, K. F., Thonnard, S. E., McCoy, R. P., & Thomas, R. J. (1997). An optical remote sensing technique for determining nighttime *F* region electron density. *Radio Science*, *32*(5), 1985–1996. https://doi.org/10.1029/97RS01887

England, S. L., Maus, S., Immel, T. J., & Mende, S. B. (2006). Longitudinal variation of the E-region electric fields caused by atmospheric tides. *Geophysical Research Letters*, *33*(21), 2006GL027465. https://doi.org/10.1029/2006GL027465

Englert, C. R., Harlander, J. M., Marr, K. D., Harding, B. J., Makela, J. J., Fae, T., et al. (2023). Michelson Interferometer for Global High-Resolution Thermospheric Imaging (MIGHTI) On-Orbit Wind Observations: Data Analysis and Instrument Performance. *Space Science Reviews*, *219*(3), 27. https://doi.org/10.1007/s11214-023-00971-1

Guo, B., Xu, J., Sun, L., Lin, Y., & Yuan, W. (2020). The Seasonal and Longitudinal Variations of Nighttime OI 135.6-nm Emission at Equatorial Ionization Anomaly Crests Observed by the DMSP/SSUSI. *Journal of Geophysical Research: Space Physics*, *125*(9). https://doi.org/10.1029/2019JA027764

Harlander, J. M., Englert, C. R., Brown, C. M., Marr, K. D., Miller, I. J., Zastera, V., et al. (2017). Michelson Interferometer for Global High-Resolution Thermospheric Imaging (MIGHTI): Monolithic Interferometer Design and Test. *Space Science Reviews*, *212*(1–2), 601–613. https://doi.org/10.1007/s11214-017-0374-4

He, M., Liu, L., Wan, W., & Wei, Y. (2011). Strong evidence for couplings between the ionospheric wave-4 structure and atmospheric tides: IONOSPHERIC WAVE-4 STRUCTURE. *Geophysical Research Letters*, *38*(14), n/a-n/a. https://doi.org/10.1029/2011GL047855

Immel, T. J., Sagawa, E., England, S. L., Henderson, S. B., Hagan, M. E., Mende, S. B., et al. (2006). Control of equatorial ionospheric morphology by atmospheric tides. *Geophysical Research Letters*, *33*(15), L15108. https://doi.org/10.1029/2006GL026161

Jiang, F., Mao, T., Zhang, X., Wang, Y.-G., Hu, X., Wang, D., et al. (2020). Observation of thermosphere and ionosphere using the ionosphere PhotoMeter (IPM) on the Chinese meteorological satellite FY-3D. *Advances in Space Research*, *66*(9), 2151–2167. https://doi.org/10.1016/j.asr.2020.07.027

Jiang, F., Mao, T., Zhang, X., Wang, Y., Fu, L., Hu, X., et al. (2020). The day-glow data application of FY-3D IPM in monitoring O/N2. *Journal of Atmospheric and Solar-Terrestrial Physics*, *205*, 105309. https://doi.org/10.1016/j.jastp.2020.105309

Kamalabadi, F., Karl, W. C., Semeter, J. L., Cotton, D. M., Cook, T. A., & Chakrabarti, S. (1999). A statistical framework for space-based EUV ionospheric tomography. *Radio Science*, *34*(2), 437–447. https://doi.org/10.1029/1998RS900026

Kamalabadi, F., Bust, G., Dymond, K., Gonzalez, S., Bernhardt, P., Chakrabarti, S., et al. (2002). Tomographic studies of aeronomic phenomena using radio and UV techniques. *Journal of Atmospheric and Solar-Terrestrial Physics*, *64*(12–14), 1573–1580. https://doi.org/10.1016/S1364-6826(02)00096-2
Kil, H., DeMajistre, R., & Paxton, L. J. (2004). *F* -region plasma distribution seen from TIMED/GUVI and its relation to the equatorial spread *F* activity: *F* -REGION PLASMA DENSITY FROM TIMED/GUVI. *Geophysical Research Letters*, *31*(5), n/a-n/a. https://doi.org/10.1029/2003GL018703
Laskar, F. I., Eastes, R. W., Martinis, C. R., Daniell, R. E., Pedatella, N. M., Burns, A. G., et al. (2020a). Early Morning Equatorial Ionization Anomaly From GOLD Observations. *Journal of Geophysical Research: Space Physics*, *125*(7). https://doi.org/10.1029/2019JA027487
Laskar, F. I., Eastes, R. W., Martinis, C. R., Daniell, R. E., Pedatella, N. M., Burns, A. G., et al. (2020b). Early Morning Equatorial Ionization Anomaly From GOLD Observations. *Journal of Geophysical Research: Space Physics*, *125*(7). https://doi.org/10.1029/2019JA027487
Li, X., Wan, W., Cao, J., & Ren, Z. (2019). Meteorological Scale Correlation Relationship of the Ionospheric Longitudinal Structure Wavenumber 4 and Upper Atmospheric Daily DE3 Tide. *Journal of Geophysical Research: Space Physics*, *124*(3), 2046–2057. https://doi.org/10.1029/2018JA026253
Li, X., Wan, W., Cao, J., Ren, Z., Key Laboratory of Earth and Planetary Physics, Institute of Geology and Geophysics, Chinese Academy of Sciences, Beijing 100029, China, School of Space and Environment, Beihang University, Beijing 100083, China, et al. (2020). Wavenumber-4 spectral component extracted from TIMED/SABER observations. *Earth and Planetary Physics*, *4*(5), 1–13. https://doi.org/10.26464/epp2020040
Lin, C. H., Hsiao, C. C., Liu, J. Y., & Liu, C. H. (2007). Longitudinal structure of the equatorial ionosphere: Time evolution of the four-peaked EIA structure: LONGITUDINAL EIA STRUCTURE. *Journal of Geophysical Research: Space Physics*, *112*(A12), n/a-n/a. https://doi.org/10.1029/2007JA012455
Lühr, H., Häusler, K., & Stolle, C. (2007). Longitudinal variation of *F* region electron density and thermospheric zonal wind caused by atmospheric tides. *Geophysical Research Letters*, *34*(16), 2007GL030639. https://doi.org/10.1029/2007GL030639
Martyn, D. F. (n.d.). Atmospheric tides in the ionosphere—I. Solar tides in the F2 region. *Proceedings of the Royal Society of London Series A, 189(1017)*, 241–260. https://doi.org/10.1098/rspa.1947.0037
Meier, R. R. (n.d.). Ultraviolet spectroscopy and remote sensing of the upper atmosphere, 185.
Meier, R. R., Picone, J. M., Drob, D., Bishop, J., Emmert, J. T., Lean, J. L., et al. (2015). Remote Sensing of Earth's Limb by TIMED/GUVI: Retrieval of thermospheric composition and temperature. *Earth and Space Science*, *2*(1), 1–37. https://doi.org/10.1002/2014EA000035
Pacheco, E. E., & Yizengaw, E. (2013). The day-to-day longitudinal variability of the global ionospheric density distribution at low latitudes during low solar activity: LONGITUDINAL VARIATIONS AT LOW LATITUDES. *Journal of Geophysical Research: Space Physics*, *118*(4), 1813–1823. https://doi.org/10.1002/jgra.50241
Pancheva, D., & Mukhtarov, P. (2010). Strong evidence for the tidal control on the longitudinal structure of the ionospheric F-region. *Geophysical Research Letters*, *37*(14), 2010GL044039. https://doi.org/10.1029/2010GL044039
Paxton, L. J., Meng, C.-I., Fountain, G. H., Ogorzalek, B. S., Darlington, E. H., Gary, S. A., et al. (1992). Special sensor ultraviolet spectrographic imager: an instrument description. In S.

Chakrabarti & A. B. Christensen (Eds.) (pp. 2–15). Presented at the San Diego ’92, San Diego, CA. https://doi.org/10.1117/12.60595
Paxton, L. J., Christensen, A. B., Humm, D. C., Ogorzalek, B. S., Pardoe, C. T., Morrison, D., et al. (1999). Global ultraviolet imager (GUVI): measuring composition and energy inputs for the NASA Thermosphere Ionosphere Mesosphere Energetics and Dynamics (TIMED) mission. In A. M. Larar (Ed.) (p. 265). Presented at the SPIE’s International Symposium on Optical Science, Engineering, and Instrumentation, Denver, CO, USA. https://doi.org/10.1117/12.366380
Paxton, L. J., Morrison, D., Zhang, Y., Kil, H., Wolven, B., Ogorzalek, B. S., et al. (2002). Validation of remote sensing products produced by the Special Sensor Ultraviolet Scanning Imager (SSUSI): a far UV-imaging spectrograph on DMSP F-16. In A. M. Larar & M. G. Mlynczak (Eds.) (pp. 338–348). Presented at the International Symposium on Optical Science and Technology, San Diego, CA. https://doi.org/10.1117/12.454268
Pedatella, N. M., Forbes, J. M., & Oberheide, J. (2008). Intra-annual variability of the low-latitude ionosphere due to nonmigrating tides. *Geophysical Research Letters*, *35*(18), 2008GL035332. https://doi.org/10.1029/2008GL035332
Ren, Z., Wan, W., Liu, L., Zhao, B., Wei, Y., Yue, X., & Heelis, R. A. (2008). Longitudinal variations of electron temperature and total ion density in the sunset equatorial topside ionosphere. *Geophysical Research Letters*, *35*(5), L05108. https://doi.org/10.1029/2007GL032998
Ren, Z., Wan, W., Liu, L., & Xiong, J. (2009). Intra-annual variation of wave number 4 structure of vertical **E** × **B** drifts in the equatorial ionosphere seen from ROCSAT-1. *Journal of Geophysical Research: Space Physics*, *114*(A5), 2009JA014060. https://doi.org/10.1029/2009JA014060
Rishbeth, H. (n.d.). Polarization fields produced by winds in the equatorial F region. *Planetary and Space Science*, (19(3)), 357–369. https:// doi.org/10.1016/0032-0633(71)90098-5
Sagawa, E., Maruyama, T., Immel, T. J., Frey, H. U., & Mende, S. B. (2003). Global view of the nighttime low-latitude ionosphere by the IMAGE/FUV 135.6 nm observations: GLOBAL VIEW OF THE EQUATORIAL IONOSPHERE. *Geophysical Research Letters*, *30*(10), n/a-n/a. https://doi.org/10.1029/2003GL017140
Scherliess, L., Thompson, D. C., & Schunk, R. W. (2008a). Longitudinal variability of low-latitude total electron content: Tidal influences. *Journal of Geophysical Research: Space Physics*, *113*(A1), 2007JA012480. https://doi.org/10.1029/2007JA012480
Scherliess, L., Thompson, D. C., & Schunk, R. W. (2008b). Longitudinal variability of low-latitude total electron content: Tidal influences: TIDAL INFLUENCES ON LOW-LATITUDE TEC. *Journal of Geophysical Research: Space Physics*, *113*(A1), n/a-n/a. https://doi.org/10.1029/2007JA012480
Sunda, S., & Vyas, B. M. (2013). Local time, seasonal, and solar cycle dependency of longitudinal variations of TEC along the crest of EIA over India. *Journal of Geophysical Research: Space Physics*, *118*(10), 6777–6785. https://doi.org/10.1002/2013JA018918
Wan, W., Xiong, J., Ren, Z., Liu, L., Zhang, M. -L., Ding, F., et al. (2010). Correlation between the ionospheric WN4 signature and the upper atmospheric DE3 tide. *Journal of Geophysical Research: Space Physics*, *115*(A11), 2010JA015527. https://doi.org/10.1029/2010JA015527
Wang D., Fu L., Jiang F., Jia N., Wang T., & D S. (2021). Inversion of Ionospheric O/N2 by Using FY-3D Ionospheric Photometer Data. *Spectroscopy and Spectral Analysis*, *41*(4), 1004–1010. https://doi.org/10.3964/j.issn.1000-0593(2021)04-1004-07

Wang, Y., Fu, L., Jiang, F., Hu, X., Liu, C., Zhang, X., et al. (2021). *Far ultraviolet airglow remote sensing measurements on Feng Yun 3D meteorological satellite* (preprint). Gases/Remote Sensing/Instruments and Platforms. https://doi.org/10.5194/amt-2021-195

Zhang, B., Fu, L., Mao, T., Hu, X., Jiang, F., Jia, N., et al. (2022). Statistical Study of Equatorial Ionospheric Anomaly after Midnight Based on FY-3(D) Ionospheric Photometer. *Atmosphere*, *13*(12), 2068. https://doi.org/10.3390/atmos13122068